JMATPRO	Journal of Advanced Materials and Processing 10 (3): 59-71, Summer 2022 http://jmatpro.iaun.iau.ir 20.1001.1.2322388.2022.10.3.6.3

Research Paper

Investigating the Effects of Boron and Zirconium on the High-Temperature Fatigue Behavior of Nimonic 105 Super Alloy

Zahra Asghary[1], Masumeh Seifollahi[2*] , Maryam Morakabati[3] , Seyed Mahdi Abbasi[4]

1. Phd Researcher, Faculty of Material and Manufacturing Technologies, Malek Ashtar University of Technology,Tehran, Iran.
2. Assistant professor, Faculty of Material and Manufacturing Technologies, Malek Ashtar University of Technology,Tehran, Iran.
3. Associate professor, Faculty of Material and Manufacturing Technologies, Malek Ashtar University of Technology,Tehran, Iran.
4. Professor, Faculty of Material and Manufacturing Technologies, Malek Ashtar University of Technology,Tehran, Iran.

ARTICLE INFO

Article history:

Received 10 April 2022
Accepted 08 June 2022
Available online 1 July 2022

Keywords:
Nimonic 105 Superalloy
High-temperature low-cycle fatigue
Fracture Surface
Boron
Zirconium

ABSTRACT

This study investigates the low-cycle fatigue of Nimonic105 alloy with boron and zirconium of 0.003-0.013 wt.% and 0.0-0.16 wt.%, respectively at 750 °C. The fatigue test results indicated that the alloy with boron of 0.013 wt.% had the highest fatigue life of 400 cycles, while the base alloy showed the lowest fatigue life of 21 cycles at 2% strain amplitudes. For the alloy with 0.16 wt.% Zr, and the alloy with 0.08 wt.% Zr and 0.006 wt.% B, cyclic-hardening occurred at a constant slope. Then, hardening followed a nonlinear procedure at a reducing rate. Finally, softening and fracture happened. For 0.013 wt.% Zr alloy, however, the diagram reached a stable state or slow cyclic-softening and failed after a relatively short period of cyclic - softening. The Coffin-Manson equations' parameters verified the increased flexibility due to the addition of B. to be a factor in improving high-temperature LCF strength. The investigation of the samples' fracture surfaces indicated that the intergranular fracture of the base alloy with the lowest fatigue life became intergranular and transgranular fracture in the alloy with 0.16 wt.% Zr content and the alloy with 0.08 wt.% Zr content and 0.006 wt.% B contents. Also, 0.013 wt.% B alloy with the highest fatigue life showed a completely transgranular fracture.

Citation: Asghary, Z.; Seifollahi, M.; Morakabati, M.; Abbasi, S.M. (2022). Investigating the Effects of Boron and Zirconium on the High-Temperature Fatigue Behavior of Nimonic 105 Super Alloy, Journal of Advanced Materials and Processing, 10 (3), 59-71. Dor: 20.1001.1.2322388.2022.10.3.6.3

[*] **Corresponding Author:**
E-Mail: m_seifollahi@mut.ac.ir

1. Introduction

Nickel-based superalloys have widely been employed in the construction of gas turbines. Nimonic105 supper alloy is one of the most used the nickel-based alloys in the gas turbine industry [1]. It considerably improves the hot tensile properties, strength, and creep resistance, as compared to the previous grades of the same superalloy groups, including Nimonic 80A and Nimonic 90 [2, 3]. It is of particular importance to investigate the properties and service life of blade superalloys, depending on whether the turbines are ground or non-ground, and on their function conditions. According to [4, 5], the service lives of ground and non-ground turbines' blades are determined based on low-cycle (LCF) fatigue and creep, respectively.

Generally, materials may undergo cyclic-softening or cyclic-softening under LCF tests at high temperatures, depending on the loading conditions. Fatigue-subjected materials typically reach stability and fracture after cyclic-softening or cyclic-softening. Hardening and softening arise from microstructural variations [6- 8]. The temperature, loading rate, and microstructure are among the most important factors affecting cyclic-softening and cyclic-softening [9]. The microstructural properties of superalloys change due to warming for a long time at high temperatures under operating conditions. According to studies, nickel-based superalloys' (111) planes as sliding bands, γ′/γ eutectic phase, voids and carbides, casting defects, and oxidation locations serve as crack nucleation locations at low temperatures. Superalloys are subjected to plastic deformation or creep deformation in the low-cycle high-temperature fracture mechanism. As a result, fatigue cracks resemble creep (grain boundary) cracks arising from continuous voids and carbides in grain boundaries. Plastic deformation is dominant, transgranular fracture occurs at low temperatures and high strains. Fatigue cracks typically have surface origins [10-14]. Antalovic et al. [15] investigated the high-temperature LCF of Rene 77 alloy at 927 °C. The results demonstrated that the grain boundary properties and matrix- and precipitate-induced crack growth were the two main factors in determining the high-temperature LCF life. Environmental effects could play important roles in both cases. Gayda et al. [16] studied the effects of B and Zr on the fatigue properties of Waspaloy superalloy at 650 °C. The results revealed that B and Zr improved the fatigue life and reduced the LCF crack growth rate by decreasing the grain size and enhancing the alloy's flexibility.

Sayou et al. research in the years 2004-2006 [17-20] evaluated the effects of B on the LCF properties of IN 718 superalloy. They found that B caused preferential separation in grain boundaries. A rise in the B content at the ambient temperature showed a small effect on the LCF life enhancement of IN 718 alloy. However, an increase in the B content to 100 ppm improved the alloy's LCF life at 650°C. The results also showed that B increased the strength of grain boundaries, changing intergranular fracture into the transgranular fracture and leading to a lower crack growth rate. Although numerous studies investigated the effects of B and Zr on the creep properties of superalloys [21-25], few studies evaluated the effects of B and Zr on the fatigue properties of superalloys. Hence, the present study investigates the effects of B and Zr on the high-temperature LCF behavior, nucleation locations, and fatigue growth path of Nimonic 105 superalloy.

2. Experiment Procedure

Four Nimonic 105 alloy types with different B and Zr contents were melted and purified in a VIM furnace and an ESR furnace, respectively. The resultant billets underwent hot rolling after homogenization. The chemical composition of the alloys was determined by optical emission spectroscopy (OES) for the main elements and inductively coupled plasma (ICP) for B and Zr, as reported in Table 1. Dissolution annealing was performed for 16 hours at 1060°C, followed by air cooling. Then, the samples underwent aging at 850 °C for 16 hours. The high-temperature LCF samples were prepared according to the ASTM E606 Standard for rolling. The samples were of a gauge length, gauge width, gauge thickness, and length of 9, 6, 3, and 80 mm, respectively. High-temperature LCF tests were performed in the form of consecutive tensile-tensile cycles. In each cycle, a strain higher than the elastic strain limit was applied at the total strain ranges of 1%, 1.5%, and 2% at 750 °C, followed by returning to zero strain. Controlled-strain tests (i.e., a constant strain variation range) were performed at a stress ratio of R=0 and the strain rate of $3*10^{-2}s^{-1}$ in the atmospheric conditions.

Table 1. The B and Zr contents (wt.%) of the alloys.

Elements	Cr	Co	Al	Ti	Mo	C	B	Zr	Ni
Base alloy	14.96	20.04	4.86	1.05	5.05	0.14	0.003	0	Bal.
B	14.78	20.25	4.03	1.21	4.84	0.15	0.013	0	Bal.
Z	14.79	20.21	4.63	1.15	4.87	0.14	0.003	0.16	Bal.
BZ	14.83	20.08	4.52	1.17	4.95	0.16	0.006	0.08	Bal.

After standard heat treatment at 850 °C for 16 hours, some samples underwent overaging at 750 °C for 500 hours to analyze the effects of B and Zr on the microstructures during high-temperature and long-term service. Then, high-temperature LCF tests were performed at a total strain range of 2% and a temperature of 750 °C. The microstructures of the samples were evaluated by an Olumpys optimal microscope and the scanning electron microscopes of SEM, VEGA, and TESCAB equipped with an EDS analyzer.

3. Results and discussion

3.1. Microstructures and precipitated phases

Fig. 1 represents the microstructures of Nimonic 105 alloys with different B and Zr contents after standard aging at 850 °C for 16 hours. The microstructure of the four alloys includes $M_{23}C_6$ and MC carbides as a continuous film in grain boundaries and large MC block carbides. B atoms cause the continuous morphology of $M_{23}C_6$ carbides in the base alloy to change discontinuously and separately in the grain boundaries of alloys B and BZ, as shown in Figs. 1b,c.

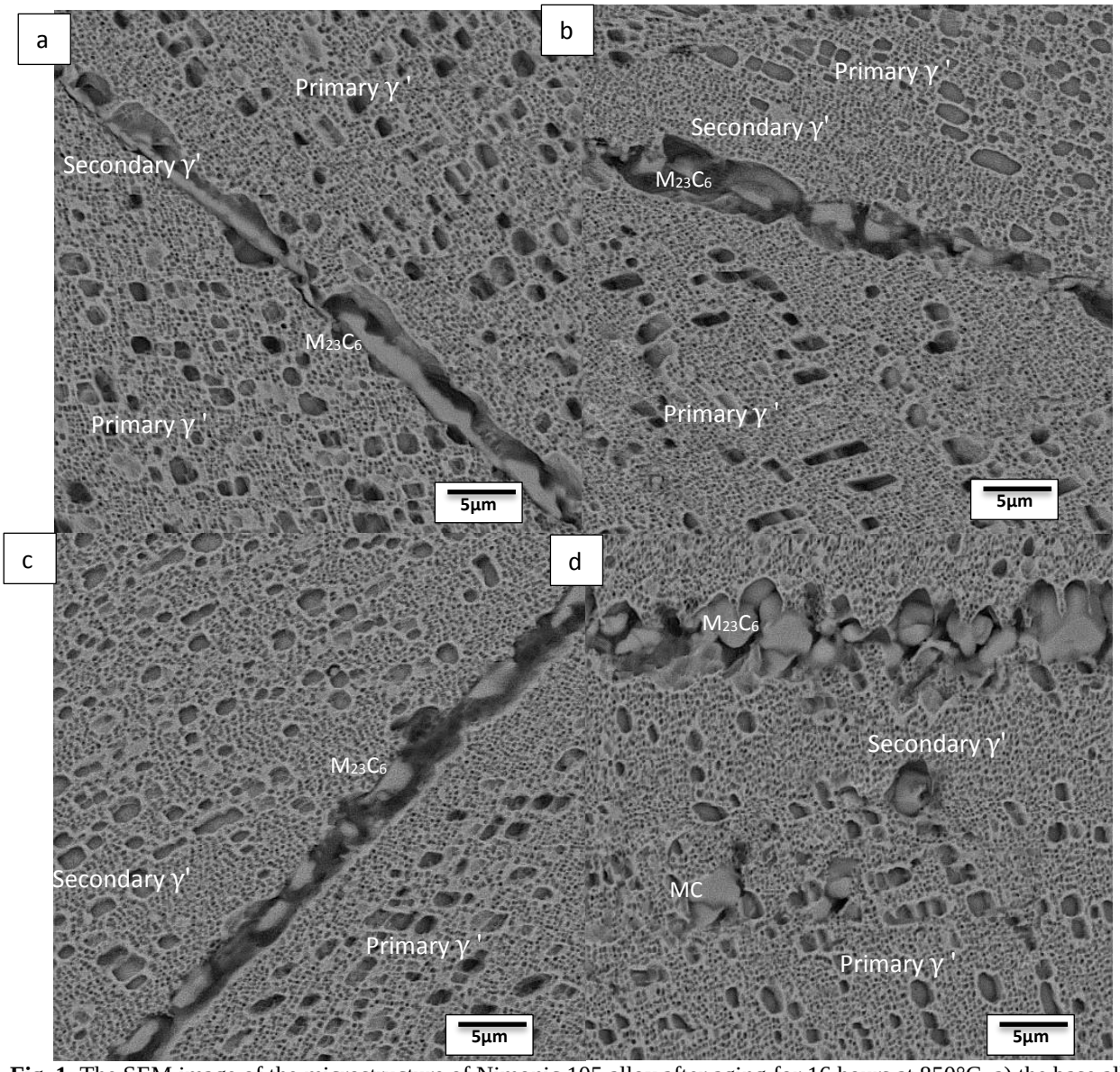

Fig. 1. The SEM image of the microstructure of Nimonic 105 alloy after aging for 16 hours at 850°C, a) the base alloy, b) alloy B, c) alloy BZ and d) alloy Z.

According to Fig. 1, there are primary and secondary γ' phases with large and small sizes in the alloys' structures. The primary γ' phase forms with a larger size after hot rolling and has sufficient opportunity to grow in different heat treatment stages. The secondary γ' phase, on the other hand, forms in the last aging stages. The addition of B and Zr reduces the primary γ' content but increases its size. The effects of B and Zr on the microstructure of this alloy were perfectly studied in [26].

3.2. High-temperature LCF in the presence of B and Zr

Fig. 2 illustrates the LCF test results for the four alloys at a strain range of 2% and a temperature of 750 °C. As can be seen, except for alloy B with a 0.013% B content, the alloys initially showed a relatively extensive period of cyclic-hardening but then underwent cyclic-softening and fracture at the strain range of 2%. Hardening and softening arise from microstructural changes. For all three alloys, hardening initially followed a constant rate but then began to continue nonlinearly at a reducing rate. The microstructural changes that cause cyclic-hardening in these alloys occurred according to Ref. [27, 28].

- Increased density and collision of dislocations (Lomer-Cottrell junctions or the formation of jogs in screw dislocations, leading to sessile dislocations), and
- The collision of dislocations and carbide precipitates (i.e., MC and $M_{23}C_6$) and the joining effects on the dislocations (i.e., the joining of dislocations by carbides).

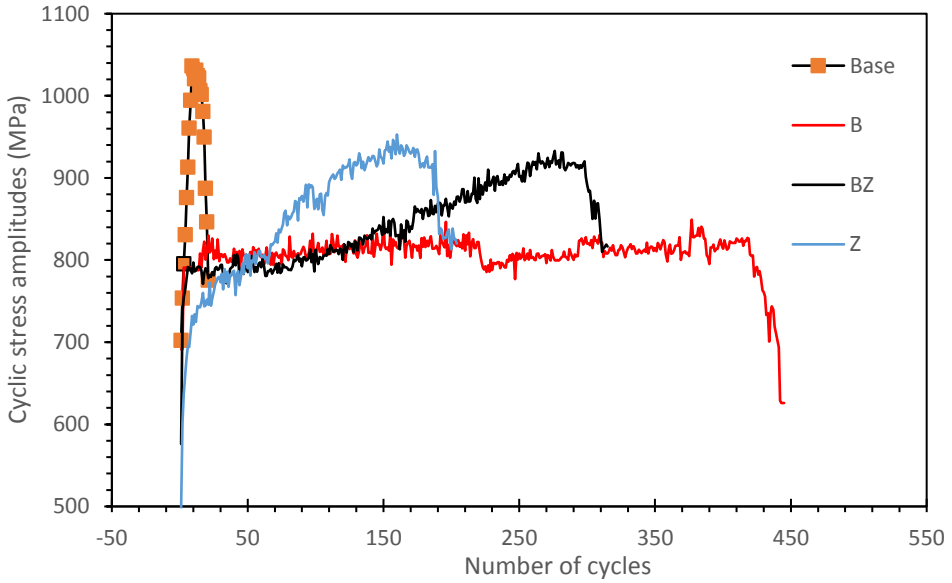

Fig. 2. The LCF results at 750 °C and a strain range of 2%.

Cyclic-hardening can result from the collision of dislocations with each other or with carbide precipitates. As a result, to maintain the applied strain, it is required to increase the flow stress to release dislocations from obstacles or create new dislocations, leading to the rise of sessile dislocations, hardening the alloy matrix, and creating initial hardening with an almost linear and constant slope. MC and $M_{23}C_6$ carbides cannot be cut by dislocations [28]. As a result, strength improves due to the presence of the carbides and thus, the creation of dislocations in the particle-matrix interface (for coarse blocks' carbides) and joining of dislocations in the light of their interaction with precipitates. This procedure was observed for the base alloy and alloys Z and BZ, with the difference that a lower cyclic-hardening was observed in alloys Z and BZ, which could be due to the change of planar and coarse TiC carbides into fine and block C carbides (Ti, Zr) in the presence of Zr (Fig. 1d) and the interruption of continuous $(Cr,Mo)_{23}C_6$ carbides in the presence of B (Fig. 1b).

However, the coherence destruction of γ' precipitates, which happens as they enlarge, is the most important reason for cyclic-softening. As coherence disappears, the cutting of participles by dislocations becomes easier. The continuous movement of dislocations in a regular lattice during cyclic strains generates atom irregularity around precipitates, contributing to the enhancement of cyclic-softening. The recovery of dislocations during fatigue tests is another procedure involved in cyclic-softening. This effect becomes larger over time. Recovery is a dynamic process of the destruction and re-arrangement of dislocations [29]. Then, the stress quickly declines due to the formation and rapid growth of cracks.

For alloy B, however, the diagram reaches stability after a relatively short cyclic-hardening period. By affecting continuous $M_{23}C_6$ carbides and changing them into discontinuous block carbides, B considerably reduced the cyclic-hardening of the alloy; cyclic-hardening arising from 'γ precipitates and cyclic-hardening due to the collision of dislocations and carbides came to equilibrium. Figs. 3 and 4 demonstrate cyclic stress range curves versus the number of cycles at different total strain ranges for the base alloy and alloy B, which represented the lowest and highest fatigue life, respectively.

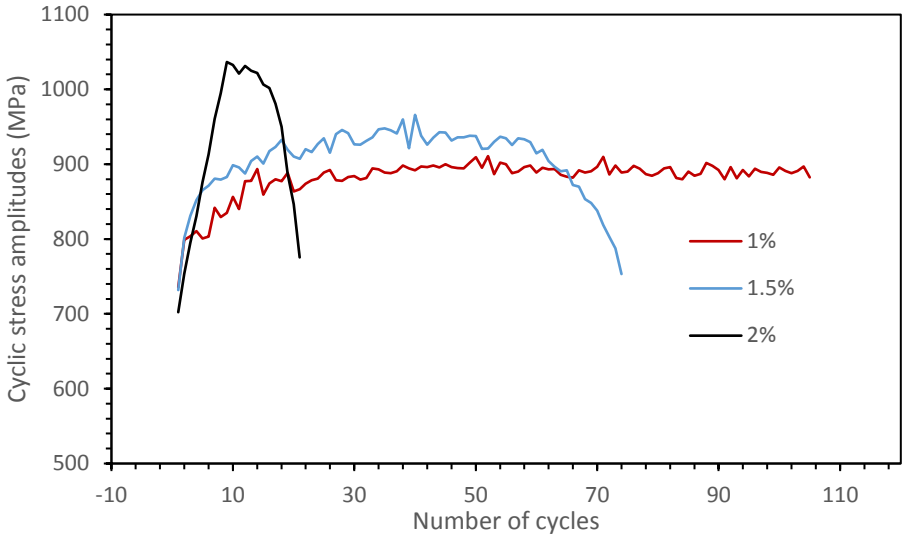

Fig. 3. Cyclic stress range curves versus the number of cycles at different total strain ranges for the base alloy.

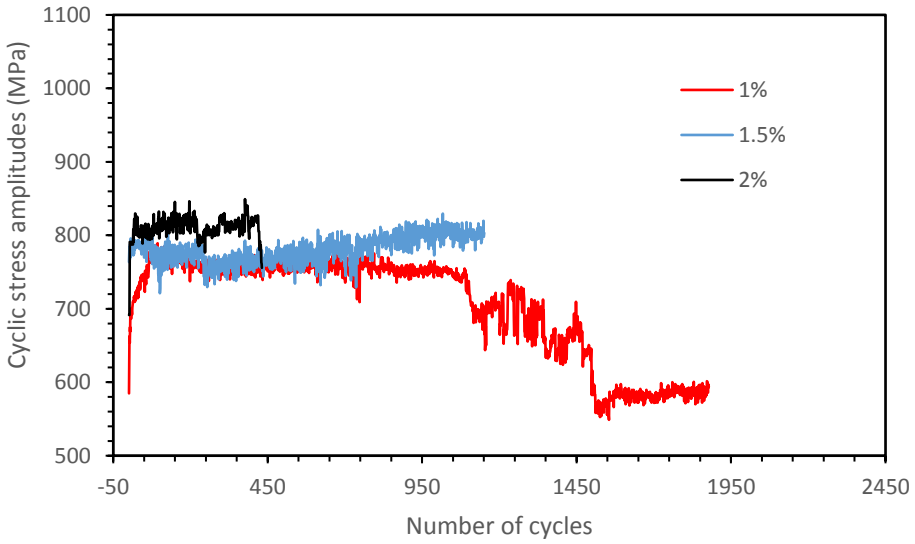

Fig. 4. Cyclic stress range curves versus the number of cycles at different total strain ranges for alloy B

Fig. 5 shows the Coffin-Manson curves of the base alloy and alloy B. The logarithmic variations of the mean plastic strain range versus the logarithmic number of cycles are represented. The fatigue flexibility coefficients and fatigue flexibility of the two alloys can be calculated by the Coffin-Manson relation and the curve tangent. Table 2 provides the two parameters' values. The fatigue flexibility coefficient also reflects tensile test flexibility to some extent and verifies increased flexibility due to adding boron in Alloy B to be a factor that improves LCF strength. Table 3 represents the tensile test results of the two alloys at 750 °C. The grain boundaries are weaker at higher temperatures, and grain boundaries serve as crack nucleation and fracture locations. As a result, the ductility of the base alloy with continuous $M_{23}C_6$ carbides in grain boundaries is considerably lower than that of alloy B. The enhancement of B content improved ductility by affecting grain boundaries. By separation on grain boundaries, B increases strength, reduces the boundary energy, and improves ductility. B also improves ductility by improving the morphology of $M_{23}C_6$ carbide precipitates into block carbides and reducing the size of grains.

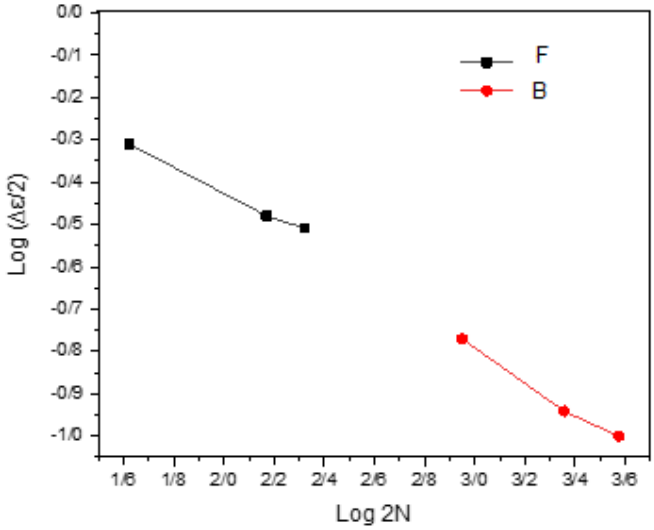

Fig. 5. The Coffin-Manson curves of the base alloy and alloy B.

Table 2. The Coffin-Manson parameters of the base alloy and alloy B.

Alloy No.	fatigue ductility exponent	fatigue ductility coefficient
Base	-0.38	0.154
B	-0.28	0.318

Table 3. The tensile properties of the base alloy and alloy B at 750°C and strain rate of 0.1 min^{-1}.

Alloy No.	Yield Strength (MPa)	Ultimate Tensile Strength (MPa)	Young's Modulus (GPa)	Elongation (%)
Base	690.5	883.3	201	16.7
B	753.8	1006.5	161	29.9

3.3. The fracture surface in the presence of B and Zr

The fracture surfaces and microstructures' side sections were investigated to analyze the fatigue cracks' nucleation locations and growth. The strongly-oxidized fracture surfaces of the samples implied the oxidation effect. In LCF, cracks begin in the form of transgranular cracks on the surface. The surface sliding and oxidation of grain boundaries are associated with the formation of fatigue cracks at high temperatures. In fact, sliding bands with high dislocation activities can serve as a penetration path for oxygen into grain boundaries [30]. However, the fatigue crack growth path can change, depending on the microstructure.

Fig. 6a shows the base alloy's fracture surface at a total strain of 2%. The destruction mechanism is merely determined by grain boundary oxidation, and no reason was observed for the fracture of the samples due to mechanical work or the proliferation of dislocations (i.e., Fatigue striations). Fig. 6b verifies that fatigue crack nucleation began with the oxides of the surface and grain boundaries, and the intergranular crack path continued as the surface cracks reached the grain boundaries and the crack path boundary oxidized. This path has the lowest fatigue life.

Fig. 6c illustrates the fracture surface of alloy B at a total strain of 2%. Fatigue striations imply that fatigue crack growth was the main cause of destruction in alloy B. The non-smooth and dimpled surfaces in Fig. 6c and transgranular cracks in Fig. 6d suggest that ductile crack growth occurred. In alloy B, transgranular fatigue cracks began to form on the surface due to the formation of surface sliding bands, and the crack growth continued transgranular as the adhesion of grain boundaries increased due to the elimination or reduction of grain boundary defects and thus, the reduction of the boundary energy and prevention of oxygen penetration into the boundaries. The fatigue striations in the fracture surface of alloy BZ in two close locations indicate the crack nucleation did not occur at only one place but began in several places, as shown in Fig. 6e. The smooth surfaces shown in Fig. 6f imply that abrupt crack growth caused the ultimate fracture.

Fig. 6g depicts the fatigue fracture surface of Alloy Z at a strain of 2%. Not only surface-near fatigue striations but also internal defect-induced crack nucleation and growth locations can be seen – the large dimples in Fig. 6g and internal cracks and voids in Fig. 6h. According to Fig. 7, crack nucleation and growth began in the interface of the matrix and carbide phase (ZrC). The meeting of surface and internal cracks can further reduce fatigue life, as compared to alloys B and BZ. The smooth surfaces in Fig. 6h demonstrate that abrupt crack growth caused the ultimate fracture.

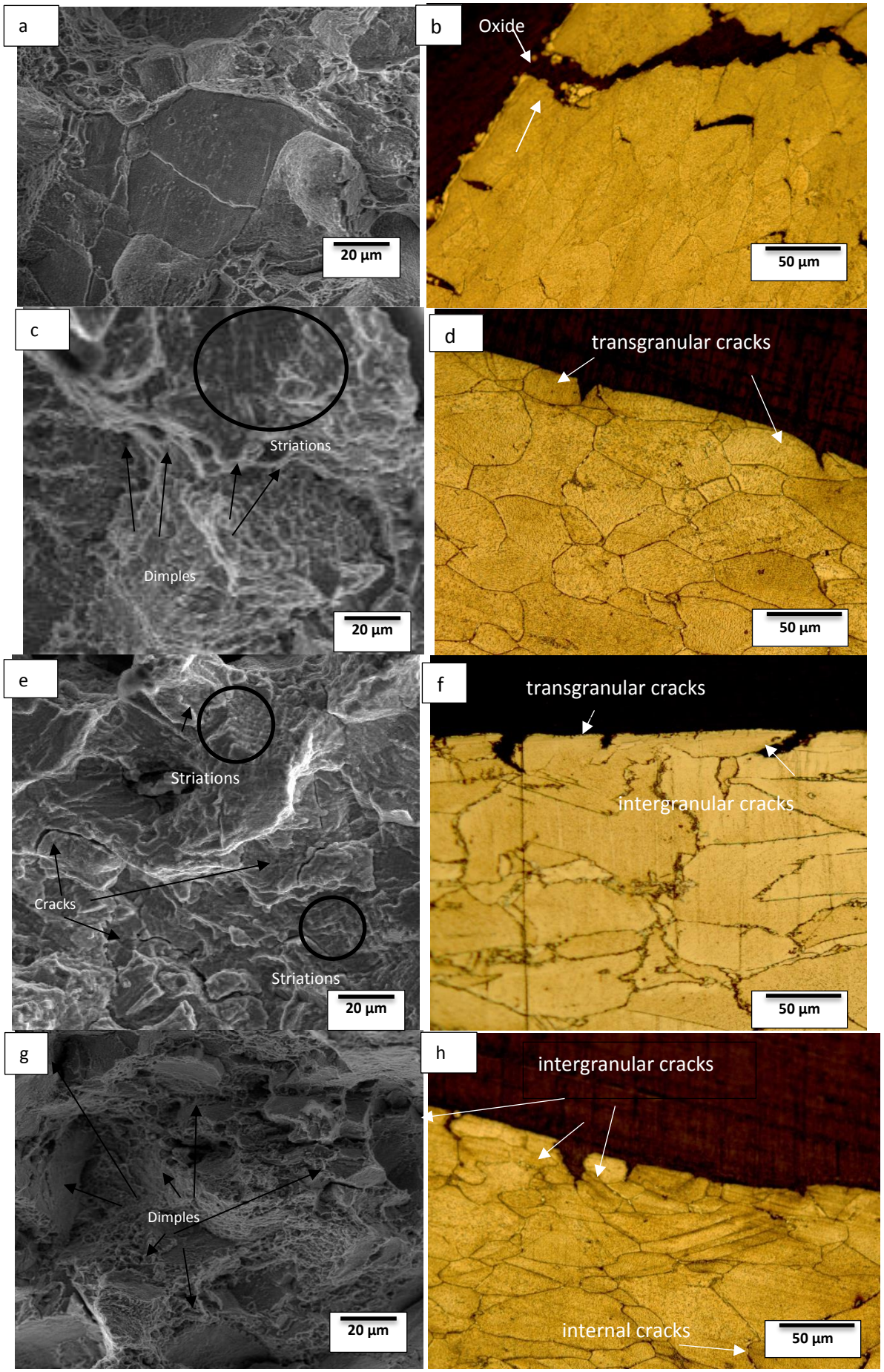

Fig. 6. The fatigue fracture surfaces and side section surfaces of a) the base alloy, b) base alloy, c) alloy B, d) alloy B, e) alloy BZ, d) alloy BZ, g) alloy Z, and h) alloy Z at 750 °C and a strain of 2%.

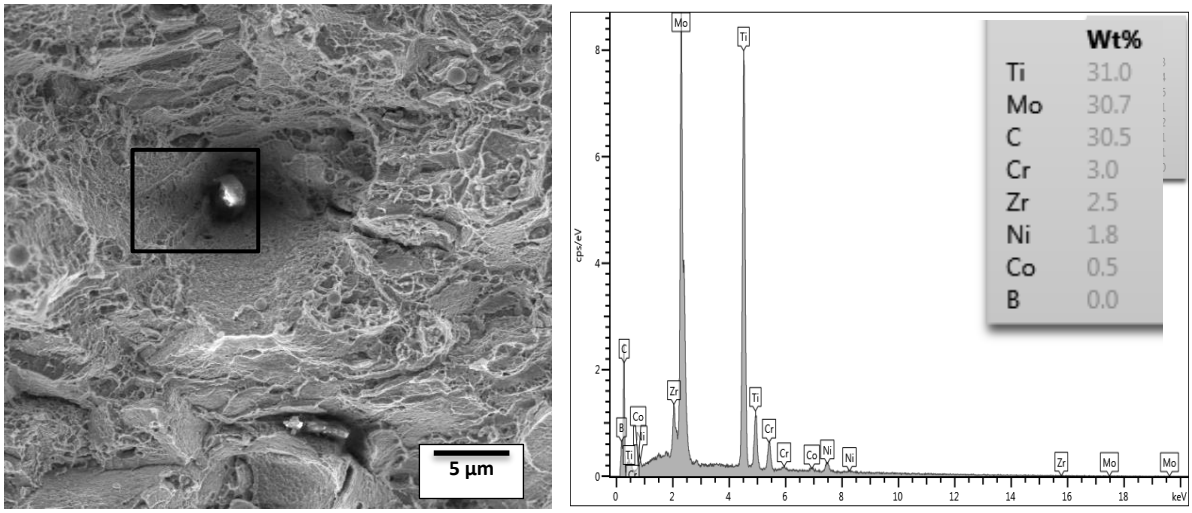

Fig. 7. The fatigue fracture surface of alloy Z along with EDS analysis results at 750 °C and a total strain of 2T

Thus, fatigue cracks begin as transgranular cracks on the surface of alloy Z. Then, the penetration of oxygen into the boundaries changed the transgranular cracks into intergranular cracks. However, unlike in the base alloy, precipitates resisted intergranular crack growth and made the fatigue cracks to be branched. As a result, alloy Z showed a larger fatigue life than the base alloy. The smooth surfaces of alloy Z are larger than those of alloy BZ. Thus, a longer life is expected for alloy BZ than for alloy Z.

Fig. 8 illustrates the fracture paths of the base alloy and alloy B. As can be seen, the base alloy has a relatively straight fracture path, while the fracture path of alloy B is non-straight. Once sliding along a group of {111} planes shifts to another group, the crack growth paths become jagged [30]. As can be seen in Fig. 8b, crystallographic facets form during crack growth, causing zigzag crack growth paths. However, no crystallographic facets are seen in the base alloy in Fig. 8a. The differences in fracture surface properties between the samples arise from microstructural properties, such as γ' precipitates and MC carbides.

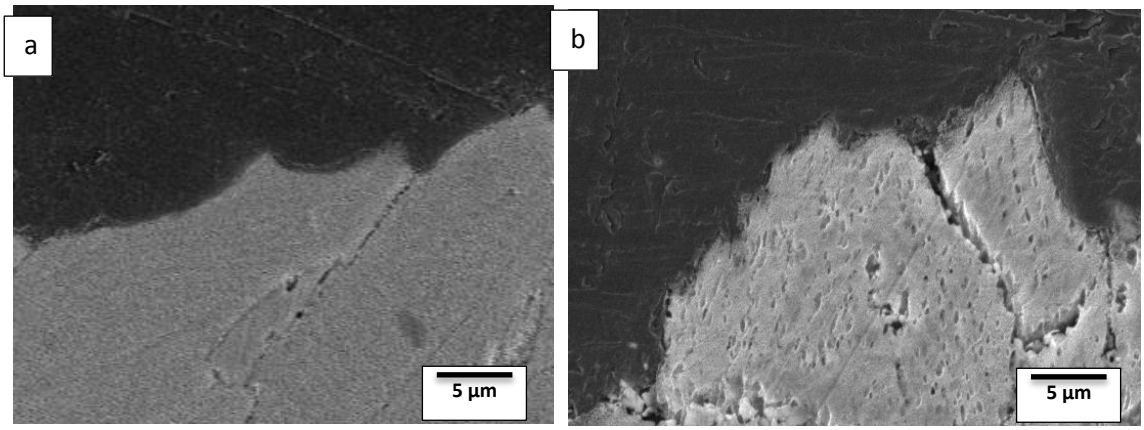

Fig. 8. The fracture path of Nimonic 105 superalloy after LCF tests at 750°C and a strain range of 2% for a) the base alloy, and b) alloy B.

A) γ' precipitates: The interaction between the γ' phase and dislocations in the plastic zone in front of crack tips influences the crack growth path. In general, small γ' precipitates are cut by dislocations, and dislocations pass through large γ' precipitates by forming an Orowan loop. The cutting mechanism changes into the mechanism of bypassing precipitates as the deposit size rises and reaches the critical value of r_c. Geometrically, the cutting model is useful for forming crystallographic facets (i.e., zigzag crack paths). Thus, shifting from cutting to bypassing due to the increased size of the γ'phase causes the fracture path to becoming smooth [31]. The critical radius for the change of the dislocation passage mechanism is calculated as follows:

$$r_c=b/\delta \quad (1)$$

where b is the Burgers vector's size, while δ is the misalignment of precipitates and the matrix. The γ' particles are cut by a/2<110> dislocations on {111} planes [32]. Once the crystalline lattice constant is known, the Burgers vector's size can be calculated as follows:

$$|b| = \frac{a}{2}\sqrt{(u^2 + v^2 + w^2)} \quad (2)$$

Asqary et al. [26] examined the XRD analysis of Nimonic 105 superalloy along with the lattice constant of the γ phase and the misalignment of the γ and γ' phases in the presence of B and Zr. By calculating the Burgers vector for the base alloy and alloys B and Z, the critical radius can be calculated for γ' precipitates, as shown in Table 4.

Table. 4. The critical radii of dislocation passage mechanism's shift from cutting to bypassing for γ' precipitates.

Type alloy	Base alloy	B	Z
a(nm)	0.3459	0.3499	0.3464
δ%	0.3951	0.4629	0.4220
b(nm)	0.2446	0.2474	0.2449
r_c(nm)	61	53	58

Given that all four alloys contained primary and secondary γ' phases and given the approximate sizes of the precipitates, as shown in Fig. 1, it can be concluded that dislocations passed through coarse primary γ' precipitates by forming Orowan loop and cut fine secondary γ' precipitates. Given that the surface fraction of primary γ' precipitates was larger in the base alloy than in alloys B and Z, B and Zr reduced the contribution of the dislocation passage mechanism by reducing the primary γ' deposit content and enhancing the contribution of deposition cutting mechanism by enhancing the stability of secondary γ' precipitates.

B) MC carbides: Dislocations aggregate near coarse carbide phases since it is difficult for dislocations to pass through carbide phases. The stress concentration due to aggregated dislocations in the non-coherent interface of the carbide phases and matrix accelerates the diffusion of cracks. Large dimples on the fracture surface (Fig. 6g) form due to transgranular and intergranular carbides and thus, the non-coherence of the interface and matrix. Fig. 7 depicts such carbides along with the EDS analysis results. The zigzag crack growth paths close roughness-induced cracks. Thus, changes in the size, type, and morphology of γ' precipitates and carbide change the crack-closing effect. As a result, the crack growth rate is affected.

Another mechanism proposed to improve the fatigue lives of alloys by adding B and Zr can be considered to be associated with grain boundary strength enhancement. Enhanced grain boundary strength reduces the grain boundary cracking tendency at high temperatures. The fracture surfaces in Fig. 6a for the base alloy demonstrate intergranular crack growth. Secondary cracks can also be observed along the grain boundaries in Fig. 6b. The lower fatigue life of alloy Z than that of alloy B can also be related to the formation of hard MC carbides that have a non-coherent interface with the matrix and grain boundaries [33]. Such carbides can provide locations for the beginning and proliferation of micro-cracks. Carbide phases easily become non-coherent in the interface and leave longitudinal dimples (Fig. 6g) in the grain boundaries and crystallographic planes immediately after sufficient strain is provided by sliding. Carbides with a non-coherent interface accelerate crack diffusion and reduce the likelihood of a change in the crack diffusion direction. For alloy B, however, a transgranular fraction with fatigue grooves is observed in Fig. 6c. The sections in Figs. 6d,f imply that a rise in the B content changes intergranular fracture into the transgranular fracture, suggesting that grain boundaries are more intergranular crack-resistant in the presence of B. Furthermore, since intergranular cracks grow considerably more rapidly than transgranular cracks, the addition of B improves fatigue life. The change from the intergranular crack fracture into the transgranular crack fracture by enhancing the B content proves that the largest contribution of B added to Nimonic 105 is the improvement of the grain boundary strength.

In addition to the fracture type, several secondary cracks on the base alloy's surface in Fig. 7 demonstrate that B and Z also influence void nucleation and crack formation. B and Zr prevent oxygen in grain boundaries. In the absence of B, the presence of oxygen in grain boundaries and the formation of interfaces with weak bonding energy make small voids stable, reducing the stress required for void formation. However, the increased B content in grain boundaries along with oxygen prevention increases the bonding energy between atoms, making the formation of voids at higher stresses possible [34].

3.4. Overaging cycle and LCF at 750°C

The overaging cycle was performed on aged alloys for 500 hours at 750 °C to simulate service conditions. Fig. 9 shows the SEM images of the alloy's microstructures after 500 hours of overaging at 750 °C. Table 5 provides the grain sizes and carbide volume fractions of the aged and overaged alloys. In addition to the increased grain sizes of the alloys that can be observed by comparing Fig. 9 to Fig. 1, the $M_{23}C_6$ carbides of alloys B and BZ became thicker than pre-aging carbides. However, they are still discontinuous, and agglomerates can be observed in the structure. Also, in addition to grain boundary $M_{23}C_6$ carbides, transgranular $M_{23}C_6$

carbides can be seen in alloy B. Furthermore, in addition to continuous carbides in grain boundaries, acicular σ phases can be observed within grains and around MC carbides in the base alloy and alloy Z. Fig. 10 represents LCF results for the alloys after 500 hours of overaging at 750 °C and a strain range of 2%. The variations of the diagrams are similar to those of the diagrams in Fig. 2, with the difference that the alloys have shorter lives. The entire alloys have higher cyclic-hardening and thus, resists larger stresses. This can be due to the increased grain size. As the grain size rises, sliding becomes more heterogeneous, and local sliding increases, enhancing cyclic-hardening. Moreover, the increased carbide deposit size and volume fraction are effective in improving the cyclic-hardening of alloys. However, in comparison to standard aging in Fig. 2, the cyclic cyclic-hardening of alloy Z considerably increased, which can be attributed to the presence of the acicular σ phase.

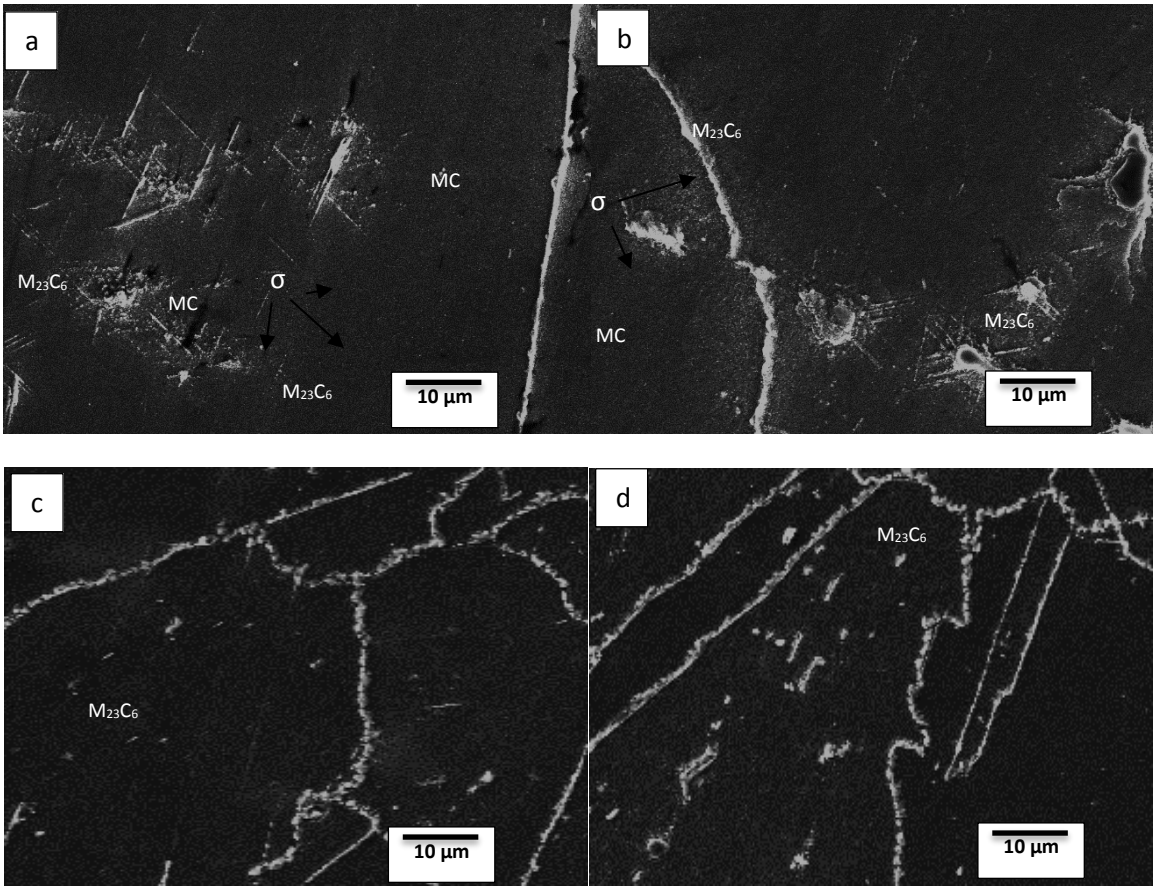

Fig. 9. The SEM images of the microstructures after 500 hours of overaging at 750°C for a) the base alloy, b) alloy Z, c) alloy B, and d) alloy BZ

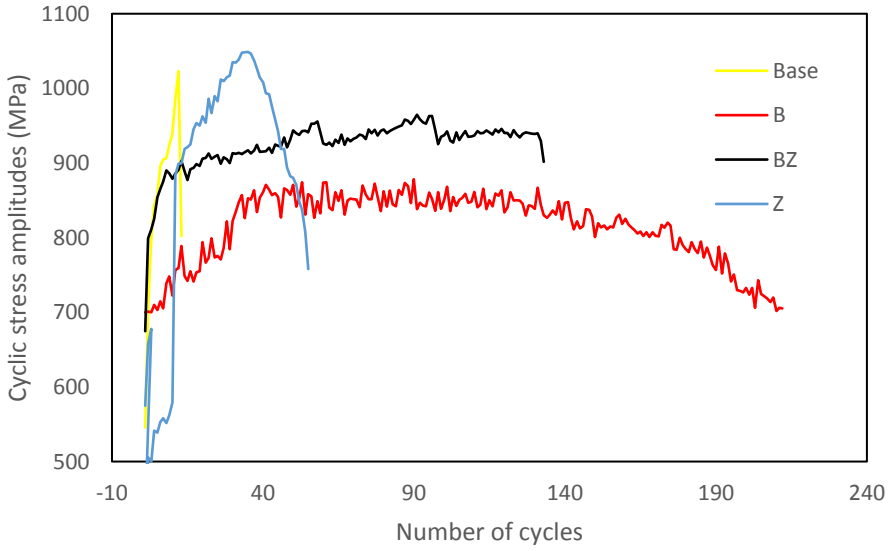

Fig. 10. LCF results at 750 °C and a strain range of 2% after 500 hours of heat treatment.

Table 5. The deposit grain size and volume fractions versus the B and Zr contents in Nimonic 105 superalloy.

Type alloy	grain size (µm)		volume fractions carbides	
	Aging 850°C-16h	Aging 850°C-16h Overaging 750°C-500h	Aging 850°C-16h	Aging 850°C -16h Overaging 750°C -500h
Base alloy	96±10	157±10	3.01±0.7	5.51±0.7
B	90±21	130±18	3.07±0.5	4.65±0.2
Z	80±6	153±10	3.67±0.7	4.98±0.8
BZ	78±11	162±6	4.16±1	5.30±0.5

Fig. 11 illustrates the fracture surface of alloy Z. The fracture surface can be divided into three zones: A) crack nucleation, B) crack growth containing several dimples, and C) complete grain boundary fracture. Zone B shows the dimples of different phases on the fracture surface of alloy Z. Round dimples cause transgranular carbide fracture and misalignment of the interface and matrix. The dimples arose from the acicular σ phases. Cracks can be observed for both types of dimples. The σ and MC phases easily become misaligned in the interface immediately after sufficient stress is provided by sliding, leaving long dimples. The TCP phases and MC carbides along with the misaligned interface accelerate crack diffusion, reducing the likelihood of a change in the crack diffusion direction.

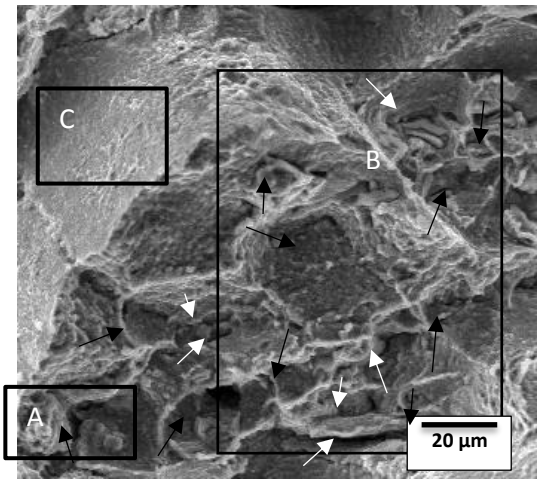

Fig. 11. The fracture surface of the base alloy after 500 hours of heat treatment at 750°C and a total strain of 2% (black arrows determine round dimples, while white arrows show stretched dimples).

4. Conclusion

- The low-cycle fatigue (LCF) results at 750°C revealed that alloy B had the longest fatigue live, followed by alloys BZ, Z, and the base allow, respectively.
- For the base alloy and alloys Z and BZ, hardening initially occurred at a constant rate but then began to continue nonlinearly at a reducing rate. For alloy B, however, the diagram reached steady state, and fractured after a relatively short period of cyclic-hardening. By affecting continuous $M_{23}C_6$ carbides and changing them into discontinuous block carbides, B considerably decreased the cyclic-hardening of alloy B.
- The fatigue flexibility coefficients and fatigue flexibility of the base alloy and alloy B were obtained by the Coffin-Manson relation and the Coffin-Manson curve's tangent. The fatigue flexibility coefficient indicated that improved flexibility due to adding B is a factor in improving LCF strength.
- The investigation of the base alloy's fracture surface at a total strain of 2% indicated that the destruction mechanism was merely determined by grain boundary oxidation, and no reason was observed for the fracture of the samples due to mechanical work or the proliferation of dislocations (fatigue striations).
- The fatigue striations in the fracture surface of alloy B at a strain of 2% implied that fatigue crack growth was the main cause of destruction. The non-smooth and dimpled surfaces on the fracture surface of alloy B demonstrated that ductile crack growth occurred.
- The fatigue fracture surface of alloy Z at a strain of 2% revealed that not only surface-near fatigue striations but also internal defects were crack nucleation and growth locations. Crack nucleation and growth began in the interface of the matrix and carbide phase (ZrC). The meeting of surface and internal cracks could further reduce the fatigue life of alloy Z, as compared to alloy B.

➢ The formation of acicular σ phases after 500 hours of overaging at 750°C in the base alloy and alloy Z enhanced their cyclic-hardening and reduced their fatigue lives.

References

[1] M. Pollock Tresa, Sammy T. "Nickel-based superalloys for advanced turbine engines: chemistry, microstructure and properties." J. propulsion power, Vol. 22, 2006, pp. 361-374.
[2] V. Seetharaman, K. Bhanu Sankara Rao, D. Sundararaman, P. Rodriguez. "Precipitation and tensile deformation behaviour of a nimonic 105 superalloy." Acta Metall., Vol. 35, 1987, pp. 565-575.
[3] N. Srinivasa, Y. V. Prasad. "Hot working characteristics of nimonic 75, 80A and 90 superalloys: a comparison using processing maps." J. Mat. Pro. Tech., Vol. 51, 1995, pp. 171-192.
[4] Y. Xu, C. Yang, X. Xiao, X. Cao, G. Jia, Z. Shen. "Strengthening behavior of Al and Ti elements at room temperature and high temperature in modified Nimonic 80A." Mat. Chem. Phys., Vol. 134, 2012, pp. 706-715.
[5] H. S. Jeong, J. R. Cho, H. C. Park. "Microstructure prediction of Nimonic 80A for large exhaust valve during hot closed die forging." Vol. 162, 2005, pp. 504-511.
[6] J. Dahal, K. Maciejewski, H. Ghonem. "Loading frequency and microstructure interactions in intergranular fatigue crack growth in a disk Ni-based superalloy." Int. J. Fat., Vol. 57, 2013, pp. 93-102.
[7] K. Obrtlík, M. Petrenec, J. Man, J. Polák, K. Hrbáček. "Isothermal fatigue behavior of cast superalloy Inconel 792-5A at 23 and 900 C." J. Mat. Sci., Vol.44, 2009, pp. 3305-3314.
[8] A. Bradley, N. Jayaraman, S. D. Antolovich. "A study of fatigue damage mechanisms in Waspaloy from 25 to 800 C." Mat. Sci. Eng., Vol. 66, 1984, pp. 151-166.
[9] S. A. Hosseini, S. M. Abbasi, K. Zangeneh Madar. "The Effect of Boron and Zirconium on the Structure and Tensile Properties of the Cast Nickel-Based Superalloy ATI 718Plus." Journal of Mat. Eng. Perform., Vol. 27, 2018, pp. 2815-2826.
[10] H. R. Jhansale, "A new parameter for the hysteretic stress-strain behavior of metals." J. Engineering Mate. Tech., Vol. 97, 1975, pp. 33-38.
[11] D. S. Antolovich, S. Liu, R. Baur. "Low cycle fatigue behavior of René 80 at elevated temperature." Metall. Trans. A, Vol. 12, 1981, pp. 473-481.
[12] S. K. Hwang, H. N. Lee, B. H. Yoon. "Mechanism of cyclic softening and fracture of a Ni-Base γ′-Strengthened alloy under low-Cycle fatigue." Metall. Trans. A, Vol. 20, 1989, pp. 2793-2801.
[13] G. R. Romanoski, S. D. Antolovich, R. M. Pelloux. "A model for life predictions of nickel-base superalloys in high-temperature low cycle fatigue." In Low Cycle Fatigue. ASTM International, 1988.
[14] K.S. Prasad, P. Ghosal, V. Kumar. "Simultaneous creep–fatigue damage accumulation of forged turbine disc of IN 718 superalloy." Mater. Sci. Eng., pp. A, Vol. 572, 2013, pp. 1-7.
[15] S. D. Antolovich, E. Rosa, A. Pineau. "Low cycle fatigue of René 77 at elevated temperatures." Mat. Sci. Eng., Vol. 47, 1981, pp. 47-57.
[16] G. John, T. P. Gabb, R. V. Miner. "Fatigue crack propagation of nickel-base superalloys at 650 C." In Low Cycle Fatigue. ASTM International, 1988.
[17] L. Xiao, D. L. Chen, M. C. Chaturvedi. "Effect of boron on fatigue crack growth behavior in superalloy IN 718 at RT and 650 C." Mat. Sci. Eng. A, Vol. 428, 2006, pp. 1-11.
[18] L. Xiao, M. C. Chaturvedi, D. L. Chen. "Effect of boron on the low-cycle fatigue behavior and deformation structure of INCONEL 718 at 650 C." Metall. Mater. Trans. A, Vol. 35, 2004, pp. 3477-3487.
[19] L. Xiao, M. C. Chaturvedi, D. L. Chen. "Effect of boron on the low-cycle fatigue behavior and deformation structure of INCONEL 718 at 650 C." Metall. Mater. Trans. A, Vol. 35, 2004, pp. 3477-3487.
[20] L. Xiao, M. C. Chaturvedi, D. L. Chen. "Low-cycle fatigue behavior of INCONEL 718 superalloy with different concentrations of boron at room temperature." Metall. Mater. Trans. A, Vol. 36, 2005, pp. 2671-2684.
[21] W.J. Pennington, "Improvement in High-Temperature Alloys by Boron and Zirconium." Metal Progr. Vol. 73, 1958.
[22] H. Huang, C. Koo. "Effect of zirconium on microstructure and mechanical properties of cast fine-grain CM 247 LC superalloy." Metall. Mater. Trans. A, Vol. 45, 2004, pp. 554-561.
[23] B. C. Yan, J. Zhang, L. H. Lou. "Effect of boron additions on the microstructure and transverse properties of a directionally solidified superalloy." Mat. Sci. Eng. A, Vol. 474, 2008, pp. 39-47.
[24] Y. Tsai, S. Wang, H. Bor, Y. Hsu. "Effects of Zr addition on the microstructure and mechanical behavior of a fine-grained nickel-based superalloy at elevated temperatures." Mat. Sci. Eng. A, Vol. 607, 2014, pp. 294-301.
[25] K. C. Antony, J. F. Radavich. "Solute effects of boron and zirconium on microporosity." In Proceedings of The Third International Symposium, Claitor Publishing. 1976.
[26] Z. Asqary, S.M. Abbasi, M. Seifollahi, M. Morakabati, "The effect of boron and zirconium on the microstructure and tensile properties of Nimonic 105 superalloy ", Mater. Res. Express, Vol. 6, 2019, pp. 1-11.

[27] M. Stucke, T. Nicholas, M. Khobaib, B. Majumdar. "Environmental aspects in creep crack growth in a nickel base superalloy." In Fracture 84, Pergamon, 1984, pp. 3967-3975.
[28] L. Wang, S. Wang, X. Song, Y. Liu, G. Xu. "Effects of precipitated phases on the crack propagation behaviour of a Ni-based superalloy." Int. J. Fatigue, Vol. 62, 2014, pp. 210-216.
[29] S.K. Hwang, H.N. Lee, B.H. Yoon. "Mechanism of cyclic softening and fracture of an Ni-Base γ′-Strengthened alloy under low-Cycle fatigue." Metall. Trans. A, Vol. 20, 1989, pp. 2793-2801.
[30] G. A. Osinkolu, G. Onofrio, M. Marchionni. "Fatigue crack growth in polycrystalline IN 718 superalloy." Mat. Sci. Eng. A, Vol. 356, 2003, pp. 425-433.
[31] H. A. Roth, C. L. Davis, R. C. Thomson. "Modeling solid solution strengthening in nickel alloys." Metall. Mater. Trans. A, Vol. 28, 1997, pp. 1329-1335.
[32] D. Krueger, S. D. Antolovich, H. R. Van Stone. "Effects of grain size and precipitate size on the fatigue crack growth behavior of alloy 718 at 427 C." Metall. Trans.s A, Vol. 18, 1987, pp. 1431-1449.
[33] T. Fedorova, J. Rösler, B. Gehrmann, J. Klöwer. "Influence of B and Zr on microstructure and mechanical properties of alloy 718." In International Symposium Superalloy 718 Derivatives, 2010, pp. 836-846.
[34] H. Ghonem, D. Zheng. "Depth of intergranular oxygen diffusion during environment-dependent fatigue crack growth in alloy 718." Mat. Sci. Eng. A, Vol. 1501992, pp. 151-160.